ACSNANO

www.acsnano.org

ARTICLE

Shape-Programmable Interfacial Solar Evaporator with Salt-Precipitation Monitoring Function

Lingyu Zhao,[⊥] Liu Wang,[⊥] Jidong Shi, Xingyu Hou, Qi Wang, Yuan Zhang, Yan Wang, Ningning Bai, Junlong Yang, Jianming Zhang, Bo Yu, and Chuan Fei Guo*

Cite This: https://dx.doi.org/10.1021/acsnano.1c01294

Read Online

ACCESS | Metrics & More | Article Recommendations | Supporting Information

ABSTRACT: **Interfacial solar evaporators (ISEs) for seawater desalination have garnered enormous attention in recent decades due to global water scarcity. Despite the progress in the energy conversion efficiency and production rate of ISE, the poor portability of large-area ISE during transportation as well as the clogging of water transport pathways by precipitated salts during operation remain grand challenges for its fielded applications. Here, we designed an ISE with high energy conversion efficiency and shape morphing capability by integrating carbon nanotube (CNT) fillers with a light-responsive shape memory polymer (SMP, cross-linked polycyclooctene (*c*PCO)). Utilizing the shape memory effect, our ISE can be folded to an origami with 1/9 of its original size to save space for transportation and allow for on-demand unfolding upon sunlight irradiation when deployed in service. In addition, the ISE is equipped with a real-time clogging monitoring function by measuring the capacitance of the electric double layer (EDL) formed at the evaporator/seawater nanointerface. Due to its good energy conversion efficiency, high portability, and clogging monitoring capability, we envisage our ISE as a promising selection in solar evaporation technologies.**

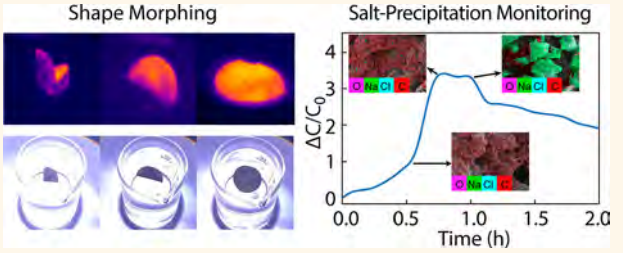

KEYWORDS: *solar evaporator, shape memory foam, salt precipitation, origami, nanointerface monitoring*

INTRODUCTION

In contrast to the abundance of seawater, the shortage of freshwater has long been a critical challenge across the world.[1,2] Massive efforts have been committed to seawater desalination in the past decades, and solar evaporation technologies have been widely studied.[3−10] To enhance the energy conversion efficiency from sunlight to water evaporation, interfacial solar evaporators (ISEs) are recently emerging with great promise by utilizing a light absorber, also known as a solar collector, floating on seawater to absorb solar energy at the liquid−air interface.[11−14] Increasing the solar absorption while reducing the heat loss is the primary consideration for the rational design of ISEs with a high energy conversion rate.[15−20] Typical solutions include developing materials with a wide solar absorption broadband and optimizing porous structures with an outstanding thermal insulation property. For example, metal nanoparticles are introduced to the absorber for more efficient light trapping enabled by surface plasmon resonance.[21] Chen et al. designed a bilayered carbon structure with porous and exfoliated graphite as the light absorber, equipped with a porous carbon foam as a thermal insulator, and achieved thermal efficiency of 85%.[22] The Hu and Zhu groups developed various water transport pathways using biomimetic structures that inhibit the thermal conduction between the absorber and the seawater.[23−25]

Despite the advances in the energy conversion efficiency of ISEs in the laboratory, two obstacles yet remain in the way to its fielded applications. First, existing ISEs are mostly made of stiff materials such as anodic aluminum oxide[26] and carbonized woods[25] that cannot be bent or folded, while the deformability and shape-morphing capability of the ISEs are captivating properties that allow for more flexibility and portability of large-scale ISEs in practice. For example, deformable ISEs with high flexibility and portability recently are emerging with great promises for practical water purification.[17,20,27,28] Although some efforts have been made to fabricate foldable and

Received: February 10, 2021
Accepted: March 3, 2021

Downloaded via SOUTHERN UNIV SCI & TECHLGY CHINA on March 9, 2021 at 05:01:00 (UTC).
See https://pubs.acs.org/sharingguidelines for options on how to legitimately share published articles.

ACS Publications

© XXXX American Chemical Society

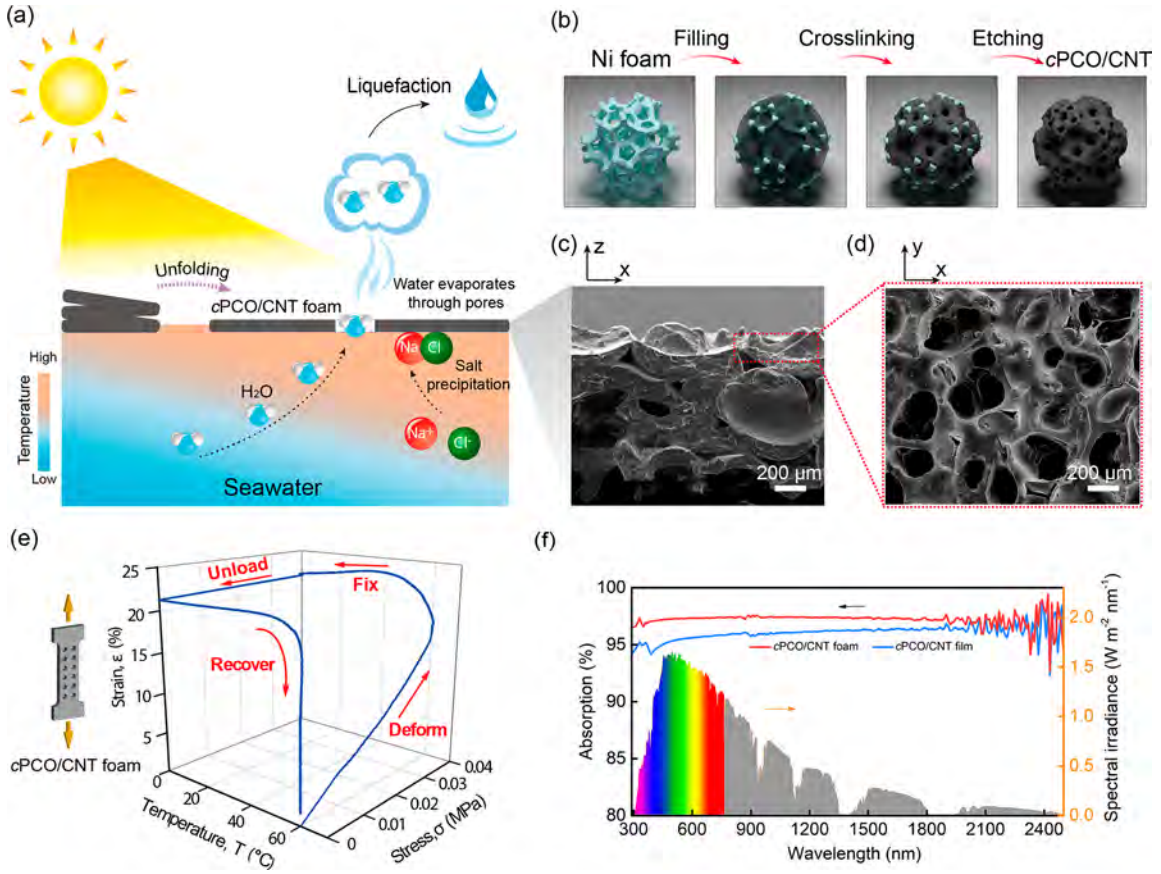

Figure 1. Principle, fabrication, and basic properties of the SMP evaporator. (a) Schematic illustration of the working mechanism for the shape-programmable solar evaporator. (b) Schematic illustration of the preparation of shape memory *c*PCO foam with Ni foam as the sacrificial template. (c) Cross-sectional scanning electron microscope (SEM) image of the *c*PCO/CNT foam. (d) Front view SEM image of a *c*PCO/CNT foam. (e) 3D diagram of shape memory cycle of the *c*PCO/CNT foam. (f) Reflection spectra of the *c*PCO/CNT film and *c*PCO/CNT foam ranging from 300 to 2500 nm.

packageable solar evaporators, the reported energy conversion efficiency was markedly low.[29] Second, as the seawater evaporates, salt precipitates inside the evaporator ducts, clogging the water transport pathway and undermining the energy absorption.[28,30] While the direct observation of salt precipitation on the IES surface may indicate the clogging to a certain degree, it fails to reveal the clogging of ducts inside. In fact, the salt precipitation on the surface may lag far behind that on the interior ducts. Although the study of salt-resistant solar evaporators has made some progress, the conversion efficiency of the photothermal material inevitably downgrades with salt participation and pollution of the surrounding environment. Determining how to monitor the evaporation efficiency of photothermal materials such that proactive acts will be taken to clean or replace the photothermal materials remains unsolved yet.[9,31] Therefore, an ISE with a high shape-morphing capability and interior clogging monitoring function while maintaining a high energy conversion rate is highly demanded.

Here, we present origami-inspired ISEs that can be folded for space-saving with an area change factor up to 9. Embodied as a shape memory polymer foam (cross-linked polycyclooctene, *c*PCO) doped with a carbon nanotube (CNT), the folded ISE can quickly heat up by absorbing solar energy, allowing for a spontaneous unfolding in merely 10 s due to the shape memory effect, as illustrated in Figure 1a. The high energy absorption of the CNT and the foam-structure-enabled low heat loss together confer our ISE a production rate of 1.26 kg m^{-2} h^{-1} and a thermal conversion efficiency of *ca.* 83% under 1 sun illumination, which is comparable to that of the state-of-the-art solar evaporators.[21−24] Furthermore, a strategy for real-time monitoring of salt precipitation in the inner pores of the foam is proposed by measuring the change in capacitance of the foam−seawater nanointerface, such that the detrimental salt precipitation could be tackled promptly before the severe clogging occurs. The excellent solar evaporation performance and a large ratio of shape morphing, together with the clogging monitoring function, make our system a promising candidate in solar evaporation technology.

RESULTS AND DISCUSSION

The shape memory *c*PCO/CNT foam was prepared through solution casting by using a commercial Ni foam as the sacrificial template, as illustrated in Figure 1b. The network structure of the Ni foam template (Figure S1) ensures interconnected pathways within the resulted *c*PCO/CNT foam after etching the metal, as shown in both the cross-sectional (Figure 1c) and the front view (Figure 1d) SEM images of the foam. The high interconnectivity of the pores ensures the transportation of water during solar evaporation. Both the thermal and the thermo-mechanical properties of the samples were studied. Differential scanning calorimeter (DSC) heat flow thermography of the linear PCO (*l*PCO) film, *c*PCO foam, *c*PCO/CNT foam, and *c*PCO/CNT film are shown in Figure S2. The melting temperature (T_m) of the samples is determined by the position

https://dx.doi.org/10.1021/acsnano.1c01294
ACS Nano XXXX, XXX, XXX−XXX

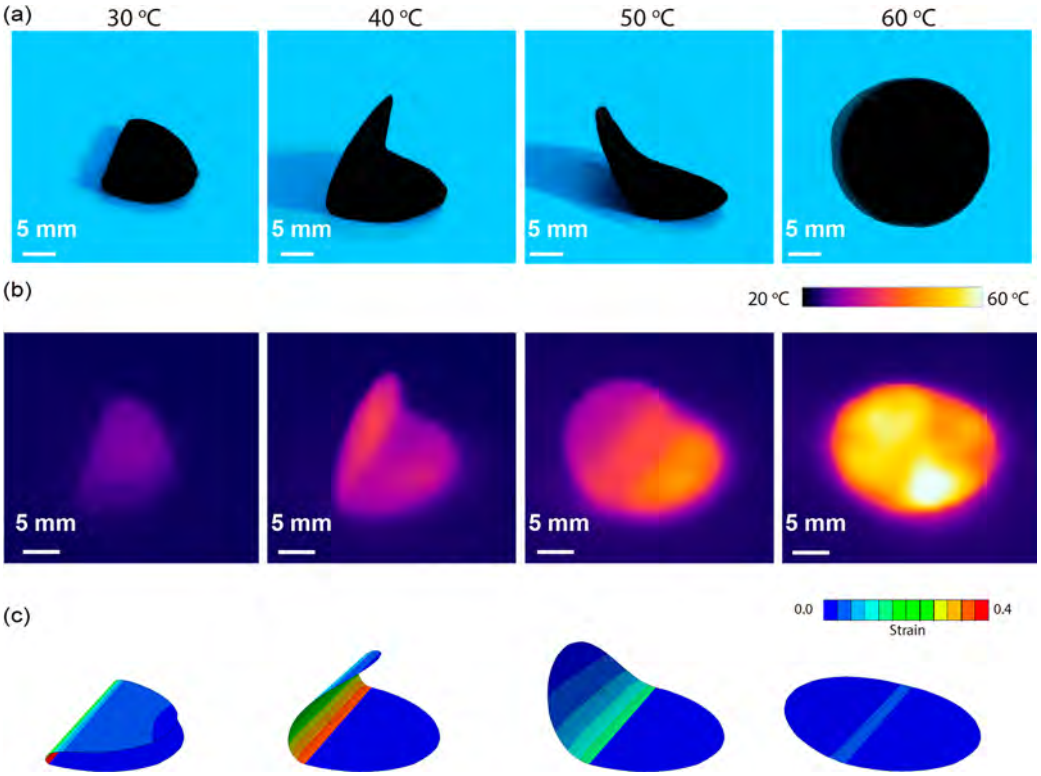

Figure 2. Shape recovery process of a *c*PCO/CNT origami under different temperatures. (a) Optical images of the origami recovered at 30, 40, 50, and 60 °C. (b) Corresponding temperature mapping of the origami. (c) Strain distribution within the origami recovered under 30, 40, 50, and 60 °C as simulated using FEM.

of the endothermic peak of each sample. For shape memory *c*PCO-based structures, T_m is also the switch temperature.[32] All T_m of the cross-linked samples are 48 °C, which is lower than that of *l*PCO (53 °C), due to the hindrance of chemical cross-linking for the crystallization of *c*PCO. The storage modulus (E') of the cross-linked samples as a function of temperature, which represents the ability of a material to store elastic deformation, was measured using a dynamic mechanical thermal analyzer. E' of all cross-linked samples decreases gradually with increasing temperature below T_m and decreases sharply at T_m. The remnant mechanical strength of the *c*PCO above T_m corresponds well with the characteristics of a cross-linked polymer (Figure S3), which shows that the mechanical stiffness of the *c*PCO foam rises by doping CNT fillers, while it decreases upon the introduction of porosity.

The strain fixity ratio (R_f) and strain recovery ratio (R_r) are two critical parameters to describe the shape memory effect of the SMP samples, expressed as follows:

$$R_f = \frac{\varepsilon_{fix}}{\varepsilon_{max}} \times 100\% \quad (1)$$

$$R_r = \frac{\varepsilon_{fix} - \varepsilon_{rec}}{\varepsilon_{fix}} \times 100\% \quad (2)$$

where ε_{max} represents the maximum strain that a SMP sample can achieve, ε_{fix} is the fixed strain after temperature cooling and stress removed, and ε_{rec} is the recovered strain after heating. The as-prepared *c*PCO/CNT foam retains the intrinsic shape memory property of *c*PCO, with a strain fixity ratio (R_f) and a strain recovery ratio (R_r) of 92% and 93% (Table S1), respectively, as calculated from the representative shape memory diagram (Figure 1e). The result demonstrates that the *c*PCO/CNT foam has an excellent shape memory effect. In addition, the absorption ratio of the *c*PCO/CNT foam dramatically grows to ~97% within both the visible and the near-infrared ranges (Figure 1f) because CNTs have a broadband absorption of solar irradiation[33] and the porous surface also favors trapping the incident light.[12]

The reasons that we chose CNTs as the fillers of the SMP are twofold. First, CNTs have great mechanical properties with a Young's modulus of 1 TPa and tensile strength up to 63 GPa,[34] which can effectively enhance the structural stiffness of the porous media and thus leads to a stronger shape memory effect. For example, the storage modulus E' of pure *c*PCO foam is merely 0.2 MPa when the temperature is above T_m (Figure S3), and R_f of the *c*PCO foam is only 78% (Table S1). By adding CNT fillers uniformly in the *c*PCO foam, the storage modulus E' and R_f are enhanced markedly to 1 MPa and 92%, respectively. Second, because of the π-band's optical transitions, CNTs have a high absorbance close to 1, resulting in an excellent absorbance capability of the *c*PCO/CNT foam with a wide broadband ranging from 300 to 2500 nm.

Origami is a type of folded structure that starts with large area flat membranes and has been proven to effectively save space in satellites by combining with shape memory materials.[35−37] The shape memory *c*PCO/CNT foam could be folded into an origami, and the unfolding behavior of the *c*PCO/CNT origami under an elevated temperature is investigated. As shown in Figure 2a, a *c*PCO/CNT origami unfolds as temperature increases from the ambient temperature to 60 °C, and corresponding temperature mapping images also well reflect this unfolding process (Figure 2b). The origami keeps the folded shape at 30 °C, starts to unfold at 40 °C, and finally flattens itself when the temperature reaches 60 °C. We carried out finite

https://dx.doi.org/10.1021/acsnano.1c01294
ACS Nano XXXX, XXX, XXX−XXX

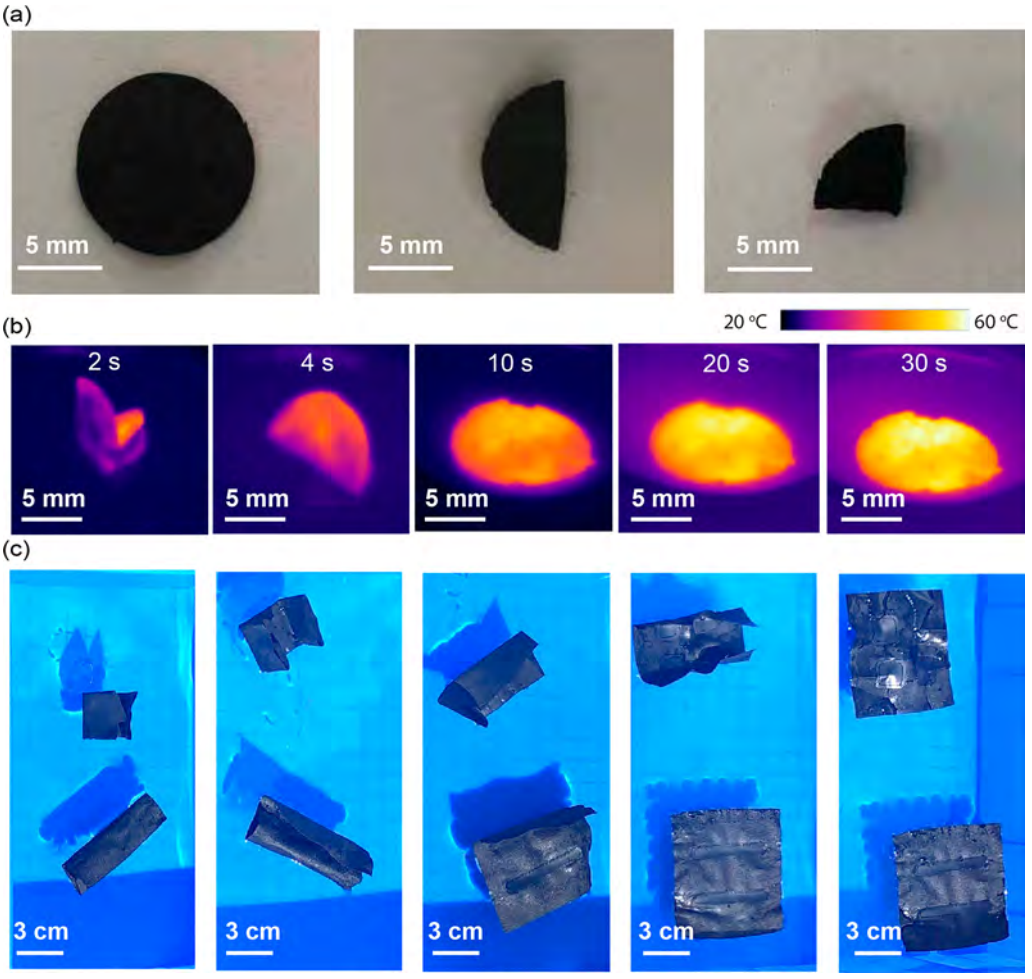

Figure 3. Spreading behavior of the *c*PCO/CNT origami under light illumination. (a) Photographs showing the folding process of a *c*PCO/CNT foam. (b) Temperature mapping of a quarter-folded origami during the spreading process. (c) Spreading process of two folded evaporators under the illumination of sunlight.

element modeling (FEM) to elucidate the shape memory process, as presented in Figure 2c. It shows that the unfolding process of the origami is accompanied by the release of compressive strain, which decreases to nearly zero at the end of the unfolding process. This is consistent with the high recovery ratio R_f mentioned above. Besides, the simulated deformation of the origami at different temperatures agrees well with our experiments, clearly showing that the shape recovery process of the origami is well controlled and predictable.

The shape recovery of the *c*PCO/CNT origami is also proven to be effective under light irradiation thanks to the superior photothermal conversion ability of the origami. A piece of circular *c*PCO/CNT foam was double folded to an origami at an elevated temperature (60 °C, Figure 3a) and then quickly cooled down to room temperature to freeze the folded state. The origami was then placed onto the water surface and irradiated using simulated sunlight. The topology and the surface temperature of the origami were real-time recorded during the unfolding process. Under 1 sun light irradiation (1 kW/m^2), the origami was quickly heated up and flattened itself (Figure 3b), with the whole process finished in only 10 s (Figure S4 and Video S1). It is also noted that evaporation simultaneously takes place during the unfolding process, as evidenced by the observed vapor in Figure S5. We further investigated the cyclic stability of the light-triggered shape recovery process. Ten cycles of repeated folding−unfolding were conducted. In each cycle, the foam was folded to half its size and unfolded under simulated sunlight. We define the folding/unfolding ratio as the projected length in the folding direction to the original length after each folding/unfolding process. During the 10 folding−unfolding cycles, the folding ratio remains at 0.5, the unfolding ratio remains at 1 (Figure S6a), and the shape recovery time is around 4 s (Figure S6b), demonstrating the high stability of our device.

The *c*PCO/CNT origami exhibits the desired shape-programmability under natural sunlight irradiation. We tested the unfolding behavior under the sunlight of ∼900 W m^{-2} to demonstrate the capability of floating *c*PCO/CNT origami evaporators to be functional in practical applications. Folded origami structures were used for this purpose, and the results are presented in Figure 3c. We show that by programming the patterns of the SMP with both biaxial folding and single-direction folding, the samples can all fully open upon sunlight irradiation. Specifically, the biaxially folded origami can significantly improve the area change ratio up to 9. This demonstration suggests a shape-programmability of our *c*PCO/CNT foam that can be folded into different shapes and allow for an on-demand expansion when deployed in service. Note that the decrease in rigidity at elevated temperatures might cause difficulties for the foam to fully open. To this end, an extra *c*PCO/CNT layer can be adhered to the creases to improve the

https://dx.doi.org/10.1021/acsnano.1c01294
ACS Nano XXXX, XXX, XXX−XXX

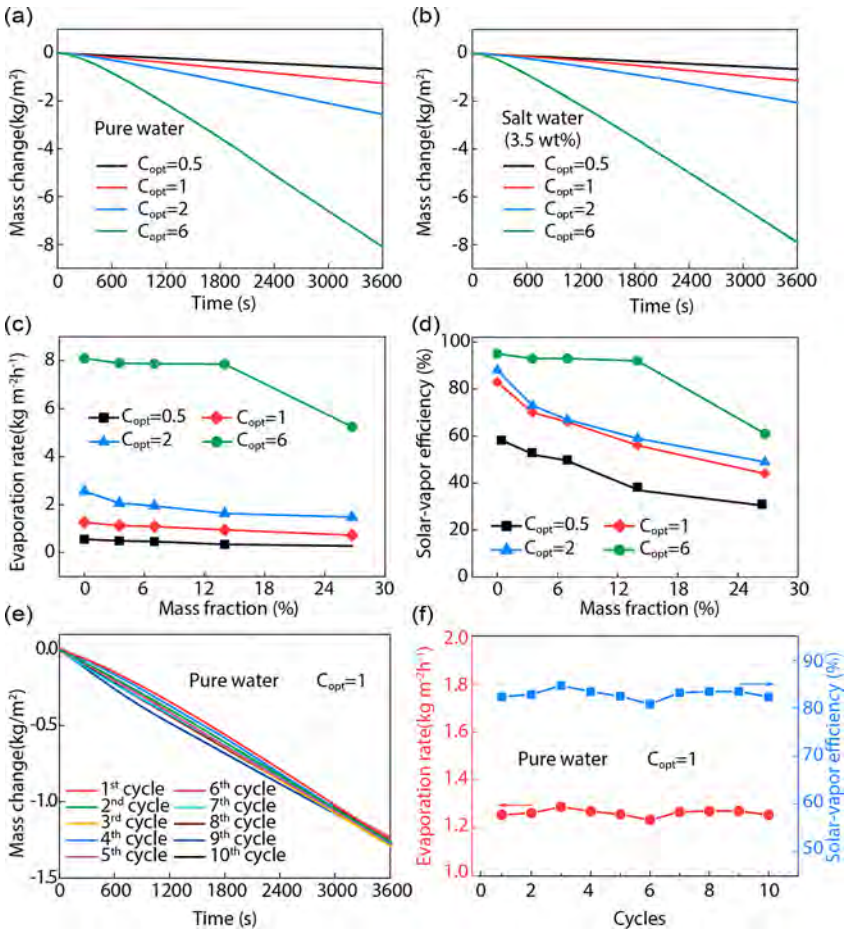

Figure 4. Solar evaporation performance of the *c*PCO/CNT foam-based evaporator. (a) Mass loss of pure water and (b) salt water (3.5 wt %) using the *c*PCO/CNT foam under different solar illumination intensities: 0.5, 1, 2, and 6 sun. (c) Evaporation rate and (d) calculated solar-to-vapor conversion efficiency of salt water with the increased mass fraction of salt. (e) Mass change of water with time over 10 evaporation cycles. (f) Evaporation rate and solar-vapor efficiency over 10 evaporation cycles.

mechanical stiffness of the origami, such that it can fully unfold when multiple creases are introduced. Our *c*PCO/CNT foam features high overall performance in terms of area change ratio and response speed compared with existing light-responsive SMPs, as summarized in Figure S7. This can be primarily attributed to the presence of CNTs, which improves not only the photothermal conversion efficiency but also the thermal conductivity within the foam, such that the whole structure could be heated up and recover to the original shape quickly.

The solar evaporation performance of the as-prepared *c*PCO/CNT foam evaporator was then investigated (Figure 4). For pure water without an evaporator, its evaporation process is rather slow under light illumination since most of the incident light is reflected or transmitted at the water/air interface (Figure S8). When the *c*PCO/CNT evaporator is placed onto the water surface, the evaporation rate has a notable improvement, which is attributed to the significantly enhanced light absorption of the *c*PCO/CNT foam and more confined heating region. The evaporation rate significantly increases with light intensity as the light intensity increases from 0.5 to 6 sun (Figure 4a). The *c*PCO/CNT evaporator also works well on simulated seawater with a salt concentration of 3.5%, with almost no decrease in the evaporation rate compared with pure water (Figure 4b). The efficiency of solar evaporation can be written as

$$\eta = \frac{mh}{Aq} \tag{3}$$

where m refers to the mass of evaporated water subtracting the mass of evaporated water under the dark field, h refers to the total liquid−vapor phase-change enthalpy, A refers to the absorption area, and q refers to the specific solar radiation power. The dependence of the water evaporation rate and solar-vapor efficiency on the light intensity are demonstrated in Figure 4c,d, respectively. The evaporation rates of pure water under 0.5, 1, 2, and 6 sun illumination are 0.55, 1.26, 2.5, and 8.1 kg m^{-2} h^{-1}, with calculated efficiencies of 59%, 83%, 88%, and 95%, respectively, indicating improved utilization of light with irradiation intensity. The evaporation rate has some decrease when the salt concentration approaches saturation, as shown in Figure 4c,d. The decrease is attributed to a well-known phenomenon that the saturated vapor pressure decreases with increasing salt concentration, called Raoult's law.[38] Since both the evaporation rates and the thermal efficiencies of the *c*PCO/CNT foam are comparable to that of the state-of-the-art solar evaporator in previous reports (Table S2), it is inferred that the introduction of the shape memory property does not downgrade the evaporation performance. The *c*PCO/CNT foam-based evaporator also exhibits excellent stability under repeated evaporation, with no performance degradation over 10 consecutive cycles (Figure 4e,f). The high conversion

https://dx.doi.org/10.1021/acsnano.1c01294
ACS Nano XXXX, XXX, XXX−XXX

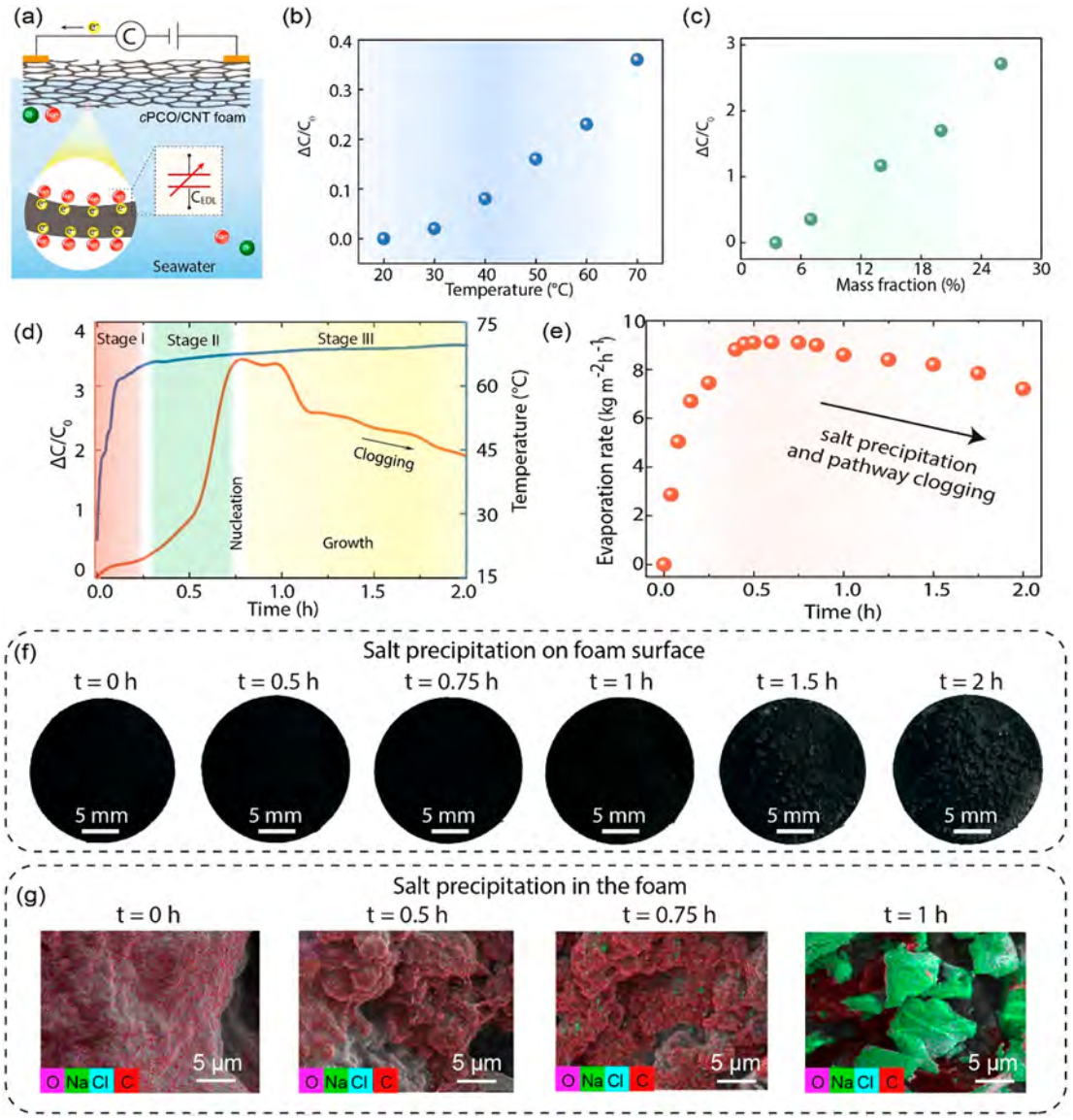

Figure 5. Real-time salt precipitation monitoring. (a) Schematic for the capacitance signal measurement. (b) Normalized change in capacitance of the 3.5% NaCl solution under different temperatures. (c) Normalized change in the capacitance of salt water with different salt concentrations (mass fractions) at 20 °C. (d) Normalized change in the capacitance and temperature of the 3.5% NaCl solution under 6 sun illumination over 2 h. (e) Evaporation rate as a function of irradiation time at 6 sun. (f) Optical images of salt precipitation on the foam surface. (g) Salt precipitation in the ducts of the foam observed by using EDS mapping. Panels (f) and (g) show that salt precipitation on the foam surface is significantly delayed.

efficiencies are attributed to the low thermal conductivity (0.0756 W m^{-1} K^{-1}) of the *c*PCO/CNT foam (Figure S9), and thus unnecessary energy waste to heat bulk water is largely avoided in our system. Besides, the pristine *c*PCO/CNT foam is hydrophobic with a contact angle of 108.9° (Figure S10a), which impairs the water transportation at the foam/water interface. To tackle this issue, we treated the foam with O_2 plasma. As a result, the contact angle decreases to 15.9° (Figure S10b), and the production rate rises from 1.02 to 1.26 kg m^{-2} h^{-1} (Figure S10c).

We also investigated the influence of the foam porosity on the evaporation performance. By varying the volume of the *c*PCO/CNT solution during the molding process, the foam porosity can be tuned accordingly as shown in Figure S11a,b. We found that both the evaporation rate and the solar-vapor efficiency first increase with the porosity and gain a maximum value when the porosity reaches 90% (Figure S11c,d). Such an increase is due to the enhanced light absorption as more *c*PCO/CNT is introduced. However, when the porosity further increases, both the evaporation rate and solar-vapor efficiency decrease. Such a decrease can be attributed to the flattening of the foam surface, which results in reduced light absorption (Figure S11e). Also, the thickness of the foam influences both the solar-vapor efficiency and the morphing capability. On the one hand, with the increase of the foam thickness, the heat flux reduced, leading to enhanced thermal insulation and higher solar-vapor efficiency.[17,23] On the other hand, increasing the thickness also increases the bending stiffness, thus impairing the shape morphing capability, given that the bending stiffness is proportional to the third order of thickness. Considering such a trade-off, in this work, the foam thickness is selected to be ~330 μm.

https://dx.doi.org/10.1021/acsnano.1c01294
ACS Nano XXXX, XXX, XXX−XXX

The solar evaporation performance degrades because the precipitation of salts clogs the water transport pathways in the *c*PCO/CNT foam, as reflected by the sharp drop in both the light absorption and production rate measured from saturated seawater under 6 sun illumination (Figure 4c,d). In practice, when the evaporator is placed on seawater, precipitated salt in the interior ducts cannot be observed; therefore, it is necessary to develop a system to monitor salt precipitation in the ducts. Since the precipitation of salt is closely related to its concentration in solution, monitoring the salt concentration is a simple but effective strategy to predict the occurrence of salt precipitation and resulted clogging of water transport pathways. An EDL forms at the foam−solution nanointerface as water is infiltrated (Figure 5a), determined by the interfacial area (which is a constant) as well as the salt concentration of the solution in the ducts. To this end, we measured the EDL capacitance using a two-probe setup (Figure 5a) which can precisely measure the change of salt concentration within the foam. We first conducted the capacitance measurement in static conditions to verify the quantitative dependence of the EDL capacitance on the salt concentration and temperature. Since the temperature rise favors the mobility of ions, the EDL capacitance also increases with increasing temperature (Figure 5b). In addition, the capacitance increases almost linearly with the salt concentration because of the increased density of the charge carriers at the interface, as shown in Figure 5c.

We conducted real-time capacitance and temperature recording during the evaporation of simulated seawater (3.5% NaCl) to monitor the clogging in the foam ducts. As shown in Figure 5d, the evaporation process can be divided into three stages (denoted as Stages I, II, and III), based on the evaluation of the capacitance and temperature of the evaporator surface. Upon light irradiation at 6 sun, the surface temperature of the foam increases rapidly from 0 to 0.25 h, denoted as Stage I, while the evaporation rate remains low. At this stage, the normalized capacitance ($\Delta C/C_0$, where ΔC is the change in the capacitance and C_0 is the initial capacitance at 20 °C) is *ca.* 0.21, and the rise is mainly due to the temperature increase, roughly in agreement with the corresponding capacitance value in Figure 5b. At Stage II (from 0.25 to 0.75 h), the temperature stabilizes at *ca.* 65 °C, while the normalized capacitance increases dramatically due to the fast water evaporation, and reaches a plateau of *ca.* 3.4 at the end of this stage, indicating that the solution inside the foam ducts is saturated. This capacitance change is quantitatively corresponding with the combined effect of increased temperature and salt concentration (Figure 5b,c), which provides a quantitative standard for the judgment of solution saturation inside the foam. Accordingly, the evaporation rate reaches its maximum at this stage (Figure 5e). At Stage III (beyond 0.75 h), the normalized capacitance has only a small decrease from 0.75 to 1 h, indicating the nucleation of salt crystals in the ducts of the foam. Likewise, the evaporation rate starts to decrease. The normalized capacitance, as well as evaporation rate, drop dramatically after 1 h, indicating the fast growth of salt particles that leads to water pathway clogging. In practical uses, the evaporator should be rinsed when the plateau of the capacitance appears.

Compared with the observation of the evaporator surface by the naked eye, the above-mentioned electrical signal monitoring method demonstrates significant advantages. From the optical images of the foam surface (Figure 5f), there are hardly traces of salt particles precipitated on the foam surface within the first hour of water evaporation. However, from the elemental distribution analysis based on SEM observation and energy dispersive spectrum (EDS) mapping within the foam ducts (Figure 5g, which more accurately reflects the salt precipitation process within the foam ducts), precipitated nanoscale salt nuclei appear at 0.75 h, and salt crystals of a few micrometers in size cover a considerable part of the surfaces of the ducts at 1 h. The EDS mapping result is in full consistency with our conclusion based on capacitance monitoring, for which capacitance shows its maximum as salt starts to nucleate at 0.75 h and significantly drops as the salt particles significantly grow up at ∼1 h. The difference between the surface optical observation and elemental analysis of the inner structures indicates that optical observation has a significant delay in determining the salt precipitation. The results discussed above validate the reliability and superiority of capacitance recording in warning of the occurrence of salt precipitation. Further efforts could be devoted to the transmission and display of the capacitance measurement results, such that people could get the warning for water transport pathway clogging promptly and take measures.

CONCLUSION

In conclusion, we have prepared a shape memory *c*PCO/CNT foam and applied it as a high-efficiency evaporator with a salt-precipitation monitoring function. The foam could be folded to form an origami with 1/9 of the original size and could fully flatten itself spontaneously under elevated temperatures or light illumination. Besides, the evaporator demonstrates high energy transfer efficiency (83% at 1 sun) and vapor productivity (1.26 kg m^{-2} h^{-1} at 1 sun). The superior performance of the evaporator lies in the high and broadband absorption of solar radiation originated from the CNTs and the porous structure, as well as the low thermal conductivity (0.0756 W m^{-1} K^{-1}) of our material to reduce the energy waste. Significantly, we developed a capacitance monitoring system utilizing the EDL capacitance of the foam−water interface. This system could warn us of the occurrence of clogging in water transport pathways, which can otherwise hardly be detected through common observation of salt precipitation on the evaporator surface. With high portability and clogging warning capability, the *c*PCO/CNT evaporator has great potential in industrial-scale vapor harvesting with high throughput and durability. Here, some limitations of the current design should also be noted. First, the area of the as-prepared evaporator is yet small. Large-area wrinkled structures can be constructed in the future for industrial applications. Second, the cost for fabricating the shape memory evaporator is 43.5 USD m^{-2} (Table S3), which is lower than evaporators made of graphene aerogel but higher than evaporators based on carbonized biochars, polypyrrole, *etc.*[21,39−42] Since the majority of the cost for evaporator preparation is the Ni foam template (Table S3), in the future, some cost-effective porous templates such as wood can be further employed.

EXPERIMENTAL SECTION

Materials. Polycyclooctene (PCO) pellets were bought from Evonik Industries AG (Germany) with a density of 0.910 g cm^{-3}. 2,5-Dimethyl-2,5-di(*tert*-butylperoxy)-hexane (DHBP) was purchased from Beijing J&K Chemical Company, China. Toluene was purchased from Shanghai Lingfeng Chemical Company, China.

Shape Memory Evaporator Preparation. First, 10 g of PCO pellets were immersed in 250 mL of toluene until they dissolved completely. A total of 0.3 g of CNT was then added to the solution,

https://dx.doi.org/10.1021/acsnano.1c01294
ACS Nano XXXX, XXX, XXX−XXX

which was stirred for 18 h to make CNT fillers disperse evenly. Then 0.2 g of DHBP was added to the solution which was stirred continuously for 1 h. Solutions with different volumes (*ca.* 2, 4, 6, 8, and 10 mL) were brushed layer by layer over the Ni foam (Lizhiyuan company, 95% porosity) with a size of 3 cm × 2.5 cm × 0.5 mm to obtain samples with different porosities. For the demonstration of the evaporation performance in Figure 4, the sample prepared by using 6 mL of solution was adopted for its optimal performance among all samples with different porosities (Figure S11). After the toluene is evaporated, the filled Ni foam was put into the hot stage at 160 °C for 20 min under gentle pressing to finish the cross-linking. Afterward, the *c*PCO/CNT/Ni foam was put into the $FeCl_3$ solution of 1 mol/L for 6 h to etch the Ni skeleton and cleaned ultrasonically to obtain the *c*PCO/CNT foam.

Characterizations. The morphological analysis of the *c*PCO/CNT was carried out by a scanning electron microscope (TESCAM MIRA3). The phase transition of the samples was analyzed by a differential scanning calorimeter (TA Instruments Q2000). The general dynamical mechanical properties of the samples were carried out on a dynamic mechanical thermal analyzer (TA Instruments Q850) in the tension mode with a temperature range from −80 to 100 °C, heating rate of 3.0 K min^{-1}, and frequency of 1 Hz. The reflectance spectra were measured in the range of 300−2500 nm by a spectrophotometer instrument (PE 950). Before the evaporation experiment, the foam was treated with O_2 plasma with a power of 100 W for 90 s. The contact angle of untreated/treated samples was measured by using a contact angle meter (AST VCA OPTIMA) with a 3 μL water droplet dropped on the foam surface. The water mass changes were measured by a balance with high accuracy (Mettler Toledo ME 204), and the real-time data could be sent to a desktop computer. The foam was folded to an origami on the hot stage at 60 °C and then rapidly cooled to room temperature to freeze the folded topology. For the spontaneous spreading of the origami, the origami was placed on water and irradiated by simulated sunlight and real sunlight. For the unfolding of the origami under real sunlight, a *c*PCO/CNT film was stitched at the crease of the origami to improve the self-unfolding force, and it could be easily exfoliated. For the conductance measurement, silver wires were attached to the two ends of the foam as electrodes, which are anchored by silver paste and encapsulated by polydimethylsiloxane (PDMS). The other ends of the silver wires were connected to an LCR meter (E4980AL, KEYSIGHT) for capacitance measurement. During the evaporation process, the capacitance of the foam could be real-time recorded.

Finite Element Simulation. Finite element simulations of shape memory behavior of the *c*PCO/CNT foam were conducted using the commercial package Abaqus 6.14. The foam is modeled as a two-dimensional shell using viscoelastic material. The relaxation modulus under various temperatures is first tested (Figure S12a) from which the master curve at a temperature of 45 °C can be constructed (Figure S12b). By fitting the experimental data using the William−Landel−Ferry (WLF) equation (Figure S12c), the shape recovery of the circular shell can be determined. The results are presented in Figure 2c.

ASSOCIATED CONTENT

Supporting Information

The Supporting Information is available free of charge at https://pubs.acs.org/doi/10.1021/acsnano.1c01294.

SEM images of the Ni foam, thermal and thermodynamic properties of the related structures, photos of the unfolding process and vapor generation, cyclic stability of the shape recovery process, comparison with other light-stimulation origami, evaporation rate of pure water without absorber, thermal conductivity of related structures, contact angles before and after plasma treatment, influence of porosities on evaporation, experimental characterization of the viscoelastic behavior (Figures S1−S12), shape memory parameters performance (Table S1), comparison of the evaporation performance with other works (Table S2), and the details of cost (Table S3) (PDF)

Video S1 recording a light-triggered shape recovery (MP4)

AUTHOR INFORMATION

Corresponding Author

Chuan Fei Guo − *Department of Materials Science and Engineering and Centers for Mechanical Engineering Research and Education at MIT and SUSTech & Shenzhen Engineering Research Center for Novel Electronic Information Materials and Devices, Southern University of Science and Technology, Shenzhen, Guangdong 518055, China;* orcid.org/0000-0003-4513-3117; Email: guocf@sustech.edu.cn

Authors

Lingyu Zhao − *Department of Materials Science and Engineering, Southern University of Science and Technology, Shenzhen, Guangdong 518055, China*

Liu Wang − *Department of Materials Science and Engineering, Southern University of Science and Technology, Shenzhen, Guangdong 518055, China*

Jidong Shi − *College of Engineering Physics, Shenzhen Technology University, Shenzhen, Guangdong 518118, China*

Xingyu Hou − *Department of Materials Science and Engineering, Southern University of Science and Technology, Shenzhen, Guangdong 518055, China*

Qi Wang − *Department of Materials Science and Engineering, Southern University of Science and Technology, Shenzhen, Guangdong 518055, China*

Yuan Zhang − *Department of Materials Science and Engineering, Southern University of Science and Technology, Shenzhen, Guangdong 518055, China*

Yan Wang − *Department of Materials Science and Engineering, Southern University of Science and Technology, Shenzhen, Guangdong 518055, China*

Ningning Bai − *Department of Materials Science and Engineering, Southern University of Science and Technology, Shenzhen, Guangdong 518055, China*

Junlong Yang − *Department of Materials Science and Engineering, Southern University of Science and Technology, Shenzhen, Guangdong 518055, China*

Jianming Zhang − *Department of Materials Science and Engineering, Southern University of Science and Technology, Shenzhen, Guangdong 518055, China*

Bo Yu − *Ningbo Fengcheng Advanced Energy Materials Research Institute, Ningbo, Zhejiang 315500, China*

Complete contact information is available at: https://pubs.acs.org/10.1021/acsnano.1c01294

Author Contributions

⊥L.Y.Z. and L.W. contributed equally to this work. C.F.G. conceived the idea. L.Y.Z. conducted the majority of the experiments. L.W. did the FEM simulations. L.Y.Z., L.W., and C.F.G. wrote and revised the manuscript with input from all other authors. All authors have approved the final version of the manuscript.

Notes

The authors declare no competing financial interest.

https://dx.doi.org/10.1021/acsnano.1c01294
ACS Nano XXXX, XXX, XXX−XXX

ACKNOWLEDGMENTS

The work was financially supported by the funds of the National Natural Science Foundation of China (No. 51771089), the "Guangdong Innovative and Entrepreneurial Research Team Program" under Contract No. 2016ZT06G587, the "Science Technology and Innovation Committee of Shenzhen Municipality" (Grant No. JCYJ20160613160524999), and the Shenzhen Sci-Tech Fund (No. KYTDPT20181011104007).

REFERENCES

(1) Mekonnen, M. M.; Hoekstra, A. Y. Four Billion People Facing Severe Water Scarcity. *Sci. Adv.* **2016**, *2*, No. e1500323.
(2) Oki, T.; Kanae, S. Global Hydrological Cycles and World Water Resources. *Science* **2006**, *313*, 1068−1072.
(3) Chen, C.; Kuang, Y.; Hu, L. B. Challenges and Opportunities for Solar Evaporation. *Joule* **2019**, *3*, 683−718.
(4) Ni, G. W.; Li, G.; Boriskina, S. V.; Li, H. X.; Yang, W. L.; Zhang, T. J.; Chen, G. Steam Generation under One Sun Enabled by a Floating Structure with Thermal Concentration. *Nat. Energy* **2016**, *1*, 16126.
(5) Zhou, L.; Tan, Y.; Ji, D.; Zhu, B.; Zhang, P.; Xu, J.; Gan, Q.; Yu, Z.; Zhu, J. Self-Assembly of Highly Efficient, Broadband Plasmonic Absorbers for Solar Steam Generation. *Sci. Adv.* **2016**, *2*, No. e1501227.
(6) Cooper, T. A.; Zandavi, S. H.; Ni, G. W.; Tsurimaki, Y.; Huang, Y.; Boriskina, S. V.; Chen, G. Contactless Steam Generation and Superheating under One Sun Illumination. *Nat. Commun.* **2018**, *9*, 5086.
(7) Cao, F.; McEnaney, K.; Chen, G.; Ren, Z. A Review of Cermet-Based Spectrally Selective Solar Absorbers. *Energy Environ. Sci.* **2014**, *7*, 1615−1627.
(8) Kabeel, A. E.; El-Agouz, S. A. Review of Researches and Developments on Solar Stills. *Desalination* **2011**, *276*, 1−12.
(9) Gao, M.; Zhu, L.; Peh, C. K.; Ho, G. W. Solar Absorber Material and System Designs for Photothermal Water Vaporization towards Clean Water and Energy Production. *Energy Environ. Sci.* **2019**, *12*, 841−864.
(10) Wu, L.; Dong, Z.; Cai, Z.; Ganapathy, T.; Fang, N. X.; Li, C.; Yu, C.; Zhang, Y.; Song, Y. Highly Efficient Three-Dimensional Solar Evaporator for High Salinity Desalination by Localized Crystallization. *Nat. Commun.* **2020**, *11*, 521.
(11) Zeng, Y.; Yao, J.; Horri, B. A.; Wang, K.; Wu, Y.; Li, D.; Wang, H. Solar Evaporation Enhancement Using Floating Light-Absorbing Magnetic Particles. *Energy Environ. Sci.* **2011**, *4*, 4074−4078.
(12) Ito, Y.; Tanabe, Y.; Han, J.; Fujita, T.; Tanigaki, K.; Chen, M. Multifunctional Porous Graphene for High-Efficiency Steam Generation by Heat Localization. *Adv. Mater.* **2015**, *27*, 4302−4307.
(13) Hu, X.; Xu, W.; Zhou, L.; Tan, Y.; Wang, Y.; Zhu, S.; Zhu, J. Tailoring Graphene Oxide-Based Aerogels for Efficient Solar Steam Generation under One Sun. *Adv. Mater.* **2017**, *29*, 1604031.
(14) Bae, K.; Kang, G.; Cho, S. K.; Park, W.; Kim, K.; Padilla, W. J. Flexible Thin-Film Black Gold Membranes with Ultrabroadband Plasmonic Nanofocusing for Efficient Solar Vapour Generation. *Nat. Commun.* **2015**, *6*, 10103.
(15) Wang, X.; Li, X.; Liu, G.; Li, J.; Hu, X.; Xu, N.; Zhao, W.; Zhu, B.; Zhu, J. An Interfacial Solar Heating Assisted Liquid Sorbent Atmospheric Water Generator. *Angew. Chem.* **2019**, *131*, 12182−12186.
(16) Yang, J.; Pang, Y.; Huang, W.; Shaw, S. K.; Schiffbauer, J.; Pillers, M. A.; Mu, X.; Luo, S.; Zhang, T.; Huang, Y.; et al. Functionalized Graphene Enables Highly Efficient Solar Thermal Steam Generation. *ACS Nano* **2017**, *11*, 5510−5518.
(17) Yang, Y.; Zhao, R.; Zhang, T.; Zhao, K.; Xiao, P.; Ma, Y.; Ajayan, P. M.; Shi, G.; Chen, Y. Graphene-Based Standalone Solar Energy Converter for Water Desalination and Purification. *ACS Nano* **2018**, *12*, 829−835.
(18) Zhao, F.; Zhou, X.; Shi, Y.; Qian, X.; Alexander, M.; Zhao, X.; Mendez, S.; Yang, R.; Qu, L.; Yu, G. Highly Efficient Solar Vapour Generation *via* Hierarchically Nanostructured Gels. *Nat. Nanotechnol.* **2018**, *13*, 489−495.
(19) Ren, H.; Tang, M.; Guan, B.; Wang, K.; Yang, J.; Wang, F.; Wang, M.; Shan, J.; Chen, Z.; Wei, D.; Peng, H.; Liu, Z. Hierarchical Graphene Foam for Efficient Omnidirectional Solar-Thermal Energy Conversion. *Adv. Mater.* **2017**, *29*, 1702590.
(20) Li, X.; Xu, W.; Tang, M.; Zhou, L.; Zhu, B.; Zhu, S.; Zhu, J. Graphene Oxide-Based Efficient and Scalable Solar Desalination under One Sun with a Confined 2D Water Path. *Proc. Natl. Acad. Sci. U. S. A.* **2016**, *113*, 13953−13958.
(21) Zhu, M.; Li, Y.; Chen, F.; Zhu, X.; Dai, J.; Li, Y.; Yang, Z.; Yan, X.; Song, J.; Wang, Y.; Hitz, E.; Luo, W.; Lu, M.; Yang, B.; Hu, L. Plasmonic Wood for High-Efficiency Solar Steam Generation. *Adv. Energy Mater.* **2018**, *8*, 1701028.
(22) Ghasemi, H.; Ni, G.; Marconnet, A. M.; Loomis, J.; Yerci, S.; Miljkovic, N.; Chen, G. Solar Steam Generation by Heat Localization. *Nat. Commun.* **2014**, *5*, 4449.
(23) Kuang, Y.; Chen, C.; He, S.; Hitz, E. M.; Wang, Y.; Gan, W.; Mi, R.; Hu, L. A High-Performance Self-Regenerating Solar Evaporator for Continuous Water Desalination. *Adv. Mater.* **2019**, *31*, 1900498.
(24) Li, X.; Lin, R.; Ni, G.; Xu, N.; Hu, X.; Zhu, B.; Lv, G.; Li, J.; Zhu, S.; Zhu, J. Three-Dimensional Artificial Transpiration for Efficient Solar Waste-Water Treatment. *Natl. Sci. Rev.* **2018**, *5*, 70−77.
(25) Zhu, M.; Li, Y.; Chen, G.; Jiang, F.; Yang, Z.; Luo, X.; Wang, Y.; Lacey, S. D.; Dai, J.; Wang, C.; Jia, C.; Wan, J.; Yao, Y.; Gong, A.; Yang, B.; Yu, Z.; Das, S.; Hu, L. Tree-Inspired Design for High-Efficiency Water Extraction. *Adv. Mater.* **2017**, *29*, 1704107.
(26) Zhou, L.; Tan, Y.; Wang, J.; Xu, W.; Yuan, Y.; Cai, W.; Zhu, S.; Zhu, J. 3D Self-Assembly of Aluminium Nanoparticles for Plasmon-Enhanced Solar Desalination. *Nat. Photonics* **2016**, *10*, 393−398.
(27) Meng, F.; Gao, M.; Ding, T.; Yilmaz, G.; Ong, W. L.; Ho, G. W. Modular Deformable Steam Electricity Cogeneration System with Photothermal, Water, and Electrochemical Tunable Multilayers. *Adv. Funct. Mater.* **2020**, *30*, 2002867.
(28) Xu, W.; Hu, X.; Zhuang, S.; Wang, Y.; Li, X.; Zhou, L.; Zhu, S.; Zhu, J. Flexible and Salt Resistant Janus Absorbers by Electrospinning for Stable and Efficient Solar Desalination. *Adv. Energy Mater.* **2018**, *8*, 1702884.
(29) Ni, G.; Zandavi, S. H.; Javid, S. M.; Boriskina, S. V.; Cooper, T. A.; Chen, G. A Salt-Rejecting Floating Solar Still for Low-Cost Desalination. *Energy Environ. Sci.* **2018**, *11*, 1510−1519.
(30) Finnerty, C.; Zhang, L.; Sedlak, D. L.; Nelson, K. L.; Mi, B. Synthetic Graphene Oxide Leaf for Solar Desalination with Zero Liquid Discharge. *Environ. Sci. Technol.* **2017**, *51*, 11701−11709.
(31) Li, J.; Zhou, X.; Chen, G.; Wang, F.; Mao, J.; Long, Y.; Sun, H.; Zhu, Z.; Liang, W.; Li, A. Evaporation Efficiency Monitoring Device Based on Biomass Photothermal Material for Salt-Resistant Solar-Driven Interfacial Evaporation. *Sol. Energy Mater. Sol. Cells* **2021**, *222*, 110941.
(32) Zhao, L. Y.; Zhao, J.; Liu, Y.; Guo, Y.; Zhang, L.; Chen, Z.; Zhang, H.; Zhang, Z. Continuously Tunable Wettability by Using Surface Patterned Shape Memory Polymers with Giant Deformability. *Small* **2016**, *12*, 3327−3333.
(33) Selvakumar, N.; Krupanidhi, S. B.; Barshilia, H. C. Carbon Nanotube-Based Tandem Absorber with Tunable Spectral Selectivity: Transition from Near-Perfect Blackbody Absorber to Solar Selective Absorber. *Adv. Mater.* **2014**, *26*, 2552−2557.
(34) Baughman, R. H.; Zakhidov, A. A.; Heer, W. A. D. Carbon Nanotubes-The Route toward Applications. *Science* **2002**, *297*, 787−792.
(35) Chen, T.; Bilal, O. R.; Lang, R.; Daraio, C.; Shea, K. Autonomous Deployment of a Solar Panel Using an Elastic Origami and Distributed Shape Memory Polymer Actuators. *Phys. Rev. Appl.* **2019**, *11*, 064069.
(36) Zhao, Z.; Wu, J.; Mu, X.; Chen, H.; Qi, H. J.; Fang, D. N. Desolvation Induced Origami of Photocurable Polymers by Digit Light Processing. *Macromol. Rapid Commun.* **2017**, *38*, 1600625.
(37) Mao, Y.; Yu, K.; Isakov, M. S.; Wu, J.; Dunn, M. L.; Qi, H. J. Sequential Self-Folding Structures by 3D Printed Digital Shape Memory Polymers. *Sci. Rep.* **2015**, *5*, 13616.
(38) Guggenheim, E. The Theoretical Basis of Raoult's Law. *Trans. Faraday Soc.* **1937**, *33*, 151−151.

https://dx.doi.org/10.1021/acsnano.1c01294
ACS Nano XXXX, XXX, XXX−XXX

(39) Hu, X.; Zhu, J. Tailoring Aerogels and Related 3D Macroporous Monoliths for Interfacial Solar Vapor Generation. *Adv. Funct. Mater.* **2020**, *30*, 1907234.
(40) Xu, N.; Hu, X.; Xu, W.; Li, X.; Zhou, L.; Zhu, S.; Zhu, J. Mushrooms as Efficient Solar Steam-Generation Devices. *Adv. Mater.* **2017**, *29*, 1606762.
(41) Zhang, L.; Tang, B.; Wu, J.; Li, R.; Wang, P. Hydrophobic Light-to-Heat Conversion Membranes with Self-Healing Ability for Interfacial Solar Heating. *Adv. Mater.* **2015**, *27*, 4889−4894.
(42) Gong, F.; Li, H.; Wang, W.; Huang, J.; Xia, D.; Liao, J.; Wu, M.; Papavassiliou, D. Scalable, Eco-Friendly and Ultrafast Solar Steam Generators Based on One-Step Melamine-Derived Carbon Sponges toward Water Purification. *Nano Energy* **2019**, *58*, 322−330.

https://dx.doi.org/10.1021/acsnano.1c01294
ACS Nano XXXX, XXX, XXX−XXX